Title

Capturing the Acoustic Radiation Pattern of Strombolian Eruptions using Infrasound Sensors Aboard a Tethered Aerostat, Yasur Volcano, Vanuatu

Journal

Geophysical Research Letters, 44(19)

ISSN

0094-8276

Authors

Jolly, Arthur D
Matoza, Robin S
Fee, David
et al.

Publication Date

2017-10-16

DOI

10.1002/2017gl074971

AGU PUBLICATIONS

Geophysical Research Letters

RESEARCH LETTER
10.1002/2017GL074971

Key Points:
- Acoustic wavefield is sampled with infrasound sensors on a tethered aerostat
- Acoustic radiation is 2 times stronger eastward of the active crater than in other directions
- Visual observations of eruptions show southeast to eastward directed ballistics for large eruptions

Supporting Information:
- Supporting Information S1
- Data Set S1
- Movie S1
- Movie S2

Correspondence to:
A. D. Jolly,
a.jolly@gns.cri.nz

Citation:
Jolly, A. D., Matoza, R. S., Fee, D., Kennedy, B. M., Iezzi, A. M., Fitzgerald, R. H., … Johnson, R. (2017). Capturing the acoustic radiation pattern of strombolian eruptions using infrasound sensors aboard a tethered aerostat, Yasur volcano, Vanuatu. *Geophysical Research Letters*, *44*, 9672–9680. https://doi.org/10.1002/2017GL074971

Received 16 JUL 2017
Accepted 14 SEP 2017
Accepted article online 25 SEP 2017
Published online 12 OCT 2017

Capturing the Acoustic Radiation Pattern of Strombolian Eruptions using Infrasound Sensors Aboard a Tethered Aerostat, Yasur Volcano, Vanuatu

Arthur D. Jolly[1], Robin S. Matoza[2], David Fee[3], Ben M. Kennedy[4], Alexandra M. Iezzi[3], Rebecca H. Fitzgerald[4], Allison C. Austin[2], and Richard Johnson[5]

[1]GNS Science, Lower Hutt, New Zealand, [2]Department of Earth Science and Earth Research Institute, University of California, Santa Barbara, CA, USA, [3]Geophysical Institute, University of Alaska Fairbanks, Fairbanks, AK, USA, [4]Department of Geological Sciences, University of Canterbury, Christchurch, New Zealand, [5]GNS Science, Wairakei Research Centre, Taupo, New Zealand

Abstract We obtained an unprecedented view of the acoustic radiation from persistent strombolian volcanic explosions at Yasur volcano, Vanuatu, from the deployment of infrasound sensors attached to a tethered aerostat. While traditional ground-based infrasound arrays may sample only a small portion of the eruption pressure wavefield, we were able to densely sample angular ranges of ~200° in azimuth and ~50° in takeoff angle by placing the aerostat at 38 tethered loiter positions around the active vent. The airborne data joined contemporaneously collected ground-based infrasound and video recordings over the period 29 July to 1 August 2016. We observe a persistent variation in the acoustic radiation pattern with average eastward directed root-mean-square pressures more than 2 times larger than in other directions. The observed radiation pattern may be related to both path effects from the crater walls, and source directionality.

1. Introduction

Volcanic eruptions include a wide range of explosivities and styles owing to the complex behavior of magmatic materials and their interaction with the shallow subsurface. Eruption directivity, where the energy and mass may be preferentially discharged from the conduit, has important hazardous consequences prompting public interest and research. Several examples of such directivity effects have been documented from visual (Lube et al., 2014), seismic (Kanamori & Given, 1982), infrasound (Jolly et al., 2014; McKee et al., 2017; Rowell et al., 2014), and GPS observations (Fournier & Jolly, 2014). Observed features of infrasonic records include seismoacoustic energy coupling and wave conversion (e.g., Johnson & Aster 2005; Ichihara et al., 2012), excitations from secondary source features such as jet turbulence (e.g., Matoza et al., 2013; Rowell et al., 2014), or distorted frequencies that may be ascribed to Doppler effects (Jolly et al., 2016). Eruption directivity effects may be associated with hazardous surge events (Lube et al., 2014), ballistics impact on infrastructure (Fitzgerald et al., 2014; Tsunematsu et al. 2016), and lateral blasts (Kanamori & Given, 1982; Kieffer, 1981); hence, the rapid recognition of such events from real-time seismoacoustic systems may someday improve response capabilities for emergency managers. Seismoacoustic records from the wide range of eruptive phenomena suffer, however, from the inherent ambiguity associated with trying to separate source directivity effects from distortions associated with path and site effects. Indeed, several studies (e.g., Kim et al., 2015; Laccana & Ripepe, 2013) indicate that topographic effects may complicate the observed waveform making isolation of source directivity features difficult.

Acoustic wavefields are a complex combination of source and propagation effects, but in a linear approximation can be represented as sums of equivalent sources: monopoles, dipoles, and quadrupoles, if the source region is compact (e.g., Pierce, 1989). The study of sound generated by fluid flow is termed aeroacoustics and its acoustic analogy theory was pioneered by Lighthill (1952, 1954, 1962, 1978). This theory was first applied to audible acoustic signals from volcanoes by Woulff and McGetchin, (1976). The applicability of this source theory to volcano infrasound was reviewed by Matoza et al. (2013), incorporating the current understanding of jet turbulence and noise. A monopole (simple) source assumption corresponds to a spherically symmetric linear acoustic source with equal radiation in all directions and is a useful first-order approximation for many short-duration volcanic explosions (e.g., Johnson et al., 2003; Kim et al., 2015). More complex volcano-acoustic sources involving sustained jet flow are hypothesized to be strongly directional with

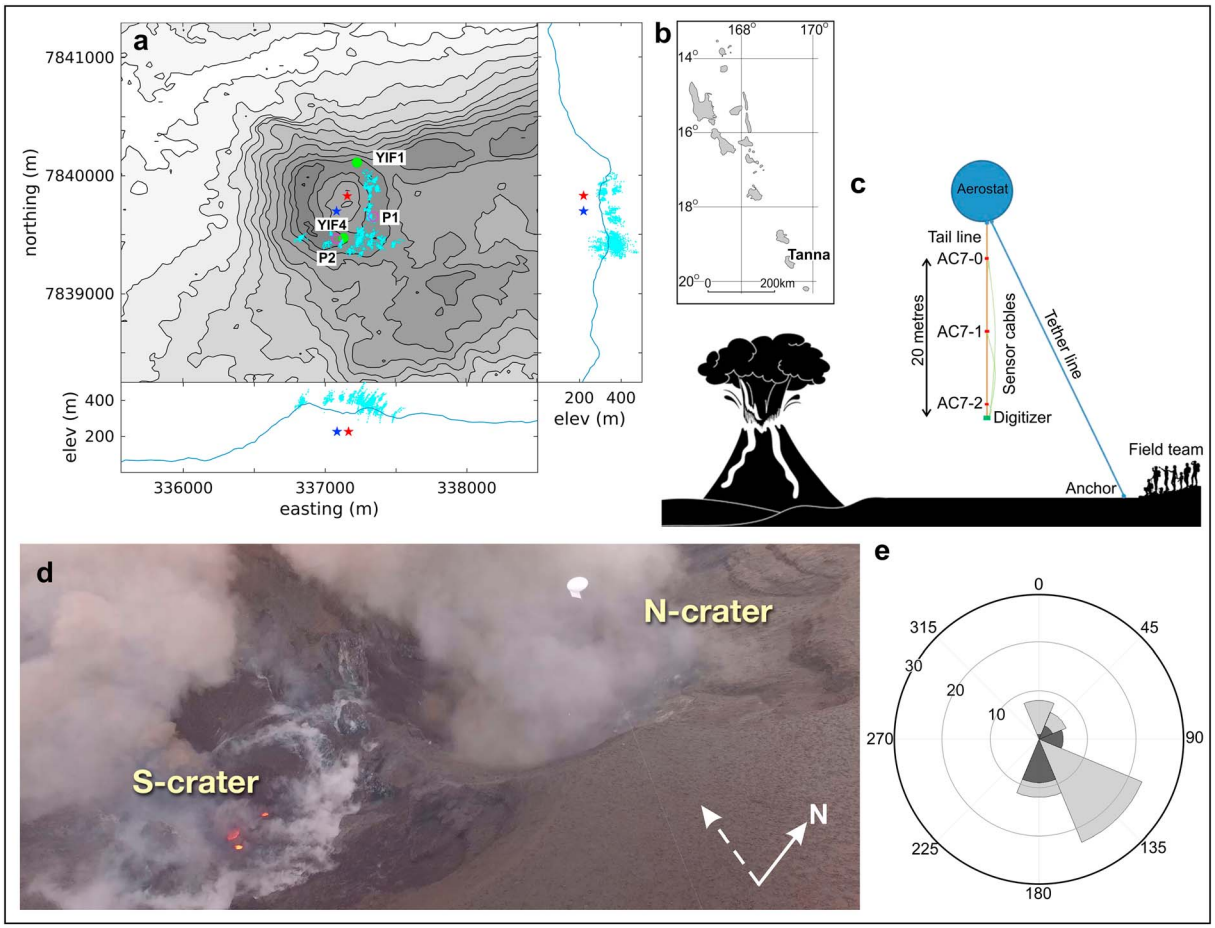

Figure 1. (a) Location map showing Yasur volcano, two ground-based infrasound sensors (YIF1 and YIF4, green dots) with north-south and east-west profiles. Aerostat locations at 20 s time intervals (cyan dots), the north crater (red star), south crater (blue star), and the position of video cameras (open red circles P1 and P2). (b) The inset map portrays Tanna Island within the South Pacific Vanuatu archipelago. (c) Aerostat setup includes a Helikite with 2–3 acoustic sensors (AC7-0, 1 and 2) on a 20 m sensor string with an Omnirecs CUBE digitizer at the base. (d) An aerial image of the north and south crater are shown with the aerostat. White arrows show north (solid) and lateral wind vector (dashed). (e) The directivity pattern measured from video (P1 and P2 in Figure 1a) for larger ballistic eruptions from S Crater (light grey) and N Crater (dark grey).

respect to angle from the jet centerline axis; however, capturing this directionality is challenging because infrasound sensors are usually located on the ground surface (Matoza et al., 2013).

The directivity features of acoustic sources have been examined in small-scale laboratory experiments (Matoza et al., 2013), from balloon and ground sensor observations of small subsurface explosions (Bowman et al., 2014), and from similar ground and air based observations for large subsurface explosions (Banister & Hereford, 1991). Rowell et al. (2014) used a three-dimensional acoustic location algorithm to study eruptive jet turbulence at Karymsky volcano, by placing sensors over a wide elevation range. The prior work shows that dipole source theory may be valid for impulsive eruptions but is probably not valid for sustained jets; basic information on the observed source directionality is needed to constrain the source theory (Matoza et al., 2013).

To better understand and constrain the directivity features of volcanic eruptions, we undertook an analysis of persistent small-scale eruptions at Yasur volcano (Figure 1a) on Tanna Island, Vanuatu (Figure 1b), South Pacific, by application of a new airborne infrasound sensor system aboard a tethered aerostat (Figure 1c). Yasur is a strombolian volcanic center that has been in continuous eruption during historical times. The volcano includes a small cone formed by deposition of ash, bombs, and lavas composed of basaltic-trachyandesite (Metrich et al., 2011) above an ash plain extending 1–3 km beyond the main vent (Figures 1a and 1b). An expedition to Yasur in September 1988 (Nairn et al., 1988) documented SO_2 gas

discharge and low-frequency earthquakes from persistent eruptive events originating from two subcraters and three main vents, a morphology that has persisted to recent times.

Recent work has focused on the visual, acoustic (Meier et al., 2016; Spina et al., 2016), and seismic aspects of the volcano and its eruptive activity (Battaglia et al., 2016; Kremers et al., 2013). The persistent degassing of exsolved magmatic gasses (Oppenheimer et al., 2006) produce gas-rich magmatic eruptions which are of limited size, allowing for visual observation of a wide range of eruption styles whose variations may be related to the vent geometry, magma dynamics, and fragmentation characteristics.

At the time of the experiment, the crater system was about 400 m wide and the maximum height of the crater rim was ~400 m above sea level. The vent depth was poorly constrained due to a lack of GPS measurements in that inaccessible portion of the volcano. However, we estimated a vent elevation of ~225 m within the northern crater vent, based on laser range to this feature from a known GPS position. The southern main vent had roughly the same elevation as the northern vent, while a third less active vent, located in the southern crater, was situated higher on the western flank of the crater wall. While the general crater morphology has persisted for more than three decades, the vent positions and naming conventions have varied over time. Hence, we simplify our naming convention to north (N) and south (S) craters within which there is some subvent evolution (Figure 1d). We exploited the persistent activity from the two crater areas and monitored the variations of the eruption energetics via ground-based infrasound sensors and a string of sensors on board a tethered aerostat (Figure 1c). We systematically moved the aerostat position to sample the range of eruption styles at a wide range of observation points (Figure 1a), hence covering an unprecedented portion of the acoustic wavefield. During the same deployment period, a set of GoPro cameras (P1 and P2 in Figure 1a) were operated intermittently and captured over 15 h of eruption footage. These observations were complemented by daily drone flights to observe vent evolution patterns (Figure 1d) and to help triangulate visual directionality of larger eruptions. For the analysis of 135 larger ballistic eruptions, distinct lateral directivity features were documented (Figure 1e) from two video cameras approximately 90° apart and subsequently compared to the distinct and persistent variation of the radiation of acoustic pressure from volcanic activity.

2. Field Method

We utilized data from two ground infrasound sensors (YIF1 and YIF4, Figure 1a) which continuously operated during the deployment period. The ground array included Chaparral Physics Model 60 UHP sensors which were sampled at a rate of 400 Hz on Omnirecs DATA-CUBE digitizers. The ground sensors have a flat response between 33 s to Nyquist and pressure range of ±1000 Pa. The airborne sensors (AC7) are InfraBSU type (Marcillo et al., 2012) with a flat response from 30 s to Nyquist and were sampled at 200 Hz on the same DATA-CUBE digitizers (Figure 1c). The aerostats were manufactured by Allsopp Helikite, hold 7 m^3 of helium, and can loft ~2 kg payload under moderate wind speeds found at Tanna. The aerostats were operated during daylight hours from 29 July to 1 August and carried two sensors for the first 3 days of operation (20 m vertical spacing) and three sensors (10 m vertical spacing) on the final day. The digitizer, having a mass of ~1 kg, served as the counterweight at the base of the sensor string (Figure 1c). Wind speed and direction were monitored using a Kestrel 5500 L anemometer located near the YIF4 station (Figure 1a) at ~1 m above the ground with a sampling period of 1 to 5 min.

The position of the infrasound sensors was derived by monitoring on-board GPS on the lofted digitizer. At the time of the experiment, the digitizer captured the latitude and longitude of the sensor but not elevation. In this case, the elevation was estimated through application of a simple Pythagorean correction, computed from the right triangle elevation knowing both the tether length and the GPS tether position (Figure 1c). Departures from a straight tether line were observed during deployment, likely due to the tether line weight and the loading effects of frictional wind drag. To improve the accuracy of the sensor altitude correction, we subsequently ran the same experimental setup in Taupo, New Zealand, under similar weather conditions and incorporated three component GPS locations via a firmware upgrade to the DATA-CUBE digitizers. The subsequent experiment measured the difference between Pythagorean and on-board GPS altitude and the corrections were applied to the Tanna deployment data.

The GPS positions for all deployments were generated at 1 Hz and sample averaged to match the window length of interest. In general, we found that 10–20 s GPS time averages yielded stable locations that

matched the known aerostat position compared to topography and ground features (e.g., summit or local topographic features). From these observations, we estimated that the aerostat locations had lateral errors of ~10 m and elevation errors of about ~15 m for the Tanna deployments. These errors are modestly smaller than the natural variation of the aerostat location at a given tethered loiter position. For the experiment, we strove to keep the aerostat below the New Zealand/Vanuatu Civil Aviation Authority (CAA) requirement of $<$110 m above topography and were usually at an elevation of 30–100 m above topography (Figure 1a).

3. Data Processing and Analysis

The airborne acoustic data were collected during daylight hours from 29 July to 1 August 2016. At approximately the same time, we collected GoPro video from positions on the southern and eastern crater rim (Figures 1a and 2a and 2b). Persistent eruptions, downwind plume conditions, and CAA regulations generally dictated the safe loiter positions for the aerostat. The local topography and volcanic hazards also prevented data collection along the northern crater rim (Figure 1a). Stationary tether anchors were established for 15–60 min which usually allowed the capture of several eruptions at each position. Over the 4 day experiment, we occupied 38 loiter positions which represented ~16 h of eruptive activity (Figures 2c–2f) during a period when the prevailing trade winds from the east-southeast were $<$10 m/s (Figure 2g) at the anemometer site noting that the wind speed at the aerostat was probably greater.

Because the activity occurred as almost continuous persistent low-level eruptions with frequent larger discrete events, we completed both continuous and event triggered analysis. For this paper, we focus on the continuous processing but note that the alternative event processing yielded similar results. For the continuous data, the two ground stations (YIF1 and YIF4) were first processed using a waveform cross-correlation approach whereby the phase lag time was determined within a time sequence of nonoverlapping 20 s windows. For each time step, the two stations are proximal to each of the active subcrater vents (Figure 1a) such that phase lag clustering of about 0.5 and -0.5 s could be distinguished and ascribed to either Crater N or S. For any 20 s period, the activity may be predominantly from one subcrater or both but the dominant subcrater was usually successfully discriminated. From this procedure, we identified 2,132 20 s windows which favored S Crater activity and 859 windows favoring N Crater activity. For each specific time window, the ground stations YIF1 and YIF4 were compared to the equivalent time window for the aerostat sensors (recorded on aerostat digitizer AC7 sensors 0, 1, and 2 (Figure 1c)). From the estimated aerostat position, the relative orientation from the active craters to aerostat-based sensors was computed, including the azimuth (Figure 2c—as viewed from the eruption crater in degrees clockwise from north), the takeoff angle (Figure 2d—as viewed from the eruption crater with vertical equal to 90°) and the straight-line source-station distance (Figure 2e).

The activity included a significant increase in eruption size and intensity beginning 1 August (Figure 2f), which corresponded to a transition from predominantly N to S Crater eruptions (Figure 2f). Over the 4 day observation period, the aerostat sensors traversed a wide range of azimuths, takeoff angles, distances, and amplitude ranges and documented the persistent features of the eruption radiation pattern.

4. Eruption Radiation Pattern

After successful discrimination of the aerostat position and vent activity, we next examined some basic features of the acoustic radiation pattern. We focused on the amplitude characteristics of the 4 day period, based on hypothesized source directivity features (e.g., Lighthill, 1978; Matoza et al., 2013). We proceeded by band-pass filtering the data (0.5–10 Hz) and then corrected the AC7 amplitudes for the aerostat-vent distance (Figure 2e) relative to the YIF4 reference station (Figure 1a). We used a geometrical decay correction ($1/r$) for a spherical source which was applied as a means to scale the ground and airborne sensors but does not account for reflective topographic effects. Next, we computed the amplitude ratio (AC7/YIF4) at each computed azimuth and takeoff angle, based on the predetermined source crater (either N or S Crater) (Figure 3). The experiment produced an uneven observation distribution around the two eruption sources, and in some cases numerous observations were taken at the same azimuth and incidence angle. To represent the over sampled regions, we gridded the graphical space into 1° increments and averaged the grid nodes that were pierced multiple times (Figures 3a and 3b). Similar results are obtained if we use station YIF1 as the reference ground station (Figures S1b and S1c in the supporting information).

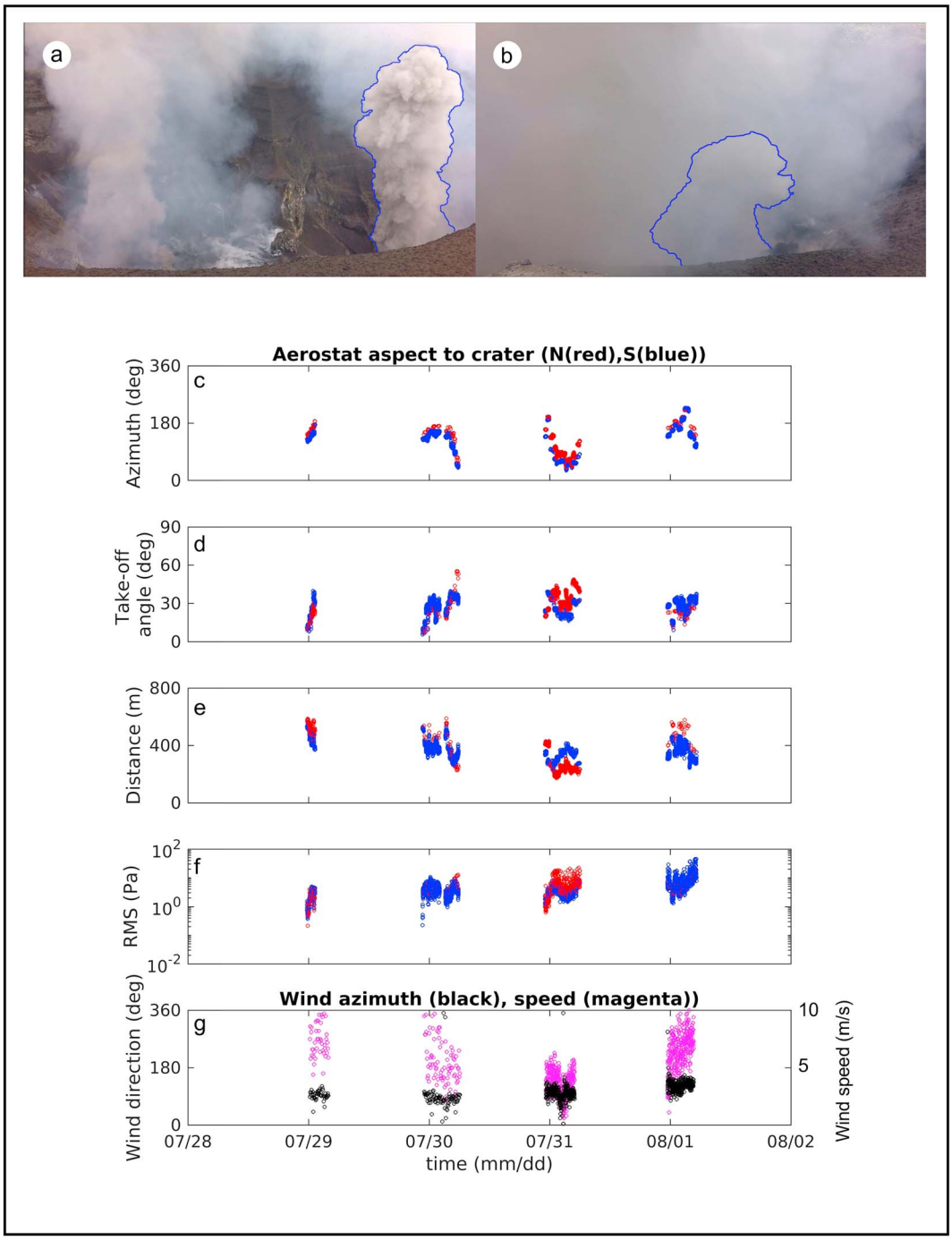

Figure 2. Example still images for eruptions from the (a) N Crater and (b) S Crater extracted from GoPro footage at positions P1 and P2, (Figure 1a). Each time step incorporates the GPS position of the aerostat (Figure 1a) allowing estimation of the (c) azimuth, (d) takeoff angle, and (e) distance relative to both active vents. (f) The RMS amplitude for the airborne sensor AC7-0. (g) The tethered aerostat position relative to the active craters was dictated by persistent trade winds, whose direction (black) and speed (magenta) were documented by a near vent anemometer (located near YIF1 in Figure 1a).

The results show a distinct and persistent high-amplitude ratio lobe located at azimuths of ~60–130° for N Crater excitations along with an increase in the amplitude ratios at higher takeoff angles. For the S Crater, the high-amplitude anomaly is also present and focused at azimuths of ~80–120°. The anomalous region was traversed over two separate days (Figure 2c) and appears to be persistent over the observation period. This anomaly is also seen for the peak amplitude from larger events (Figure S2), but the data coverage is very

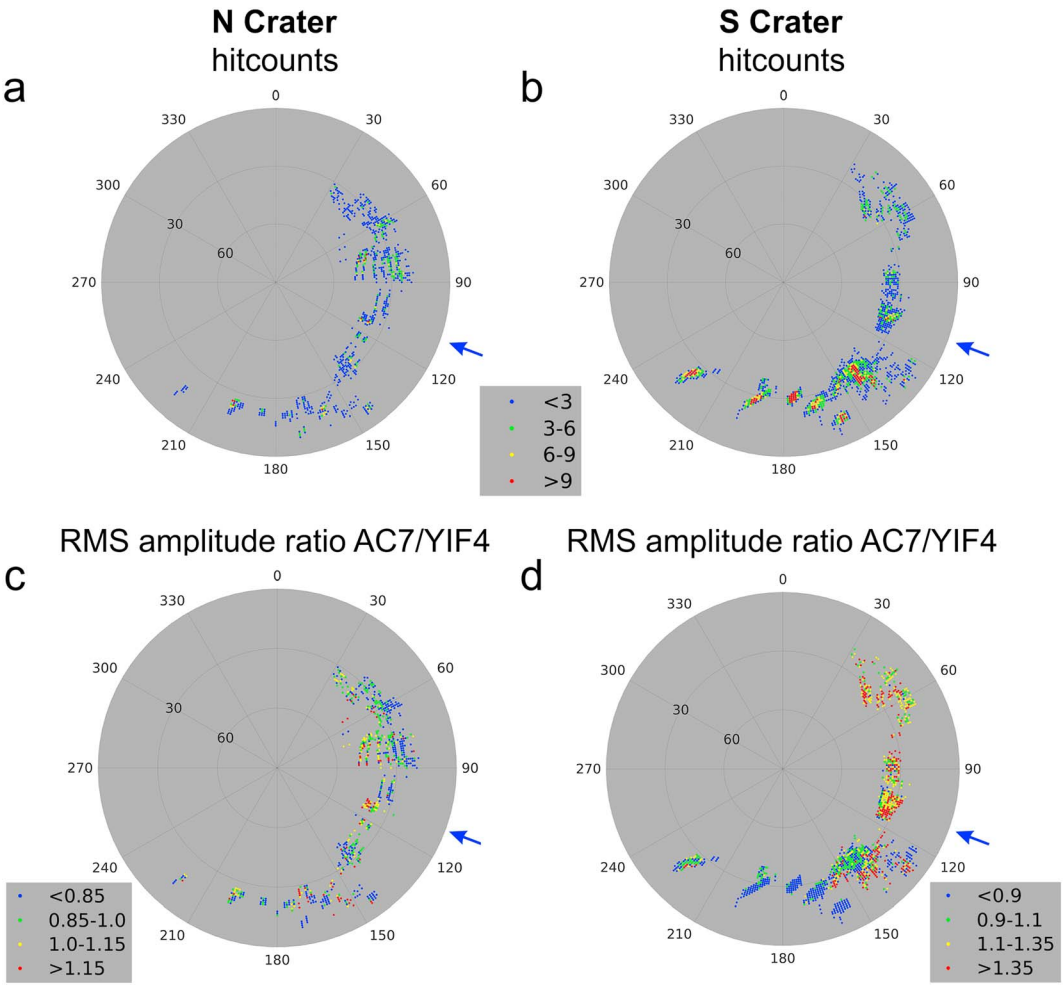

Figure 3. (a and b) Hit counts and (c and d) amplitude ratio for N Crater (Figures 3a and 3c) and S Crater (Figures 3b and 3d) activity. For each time step, the ratio (legend) is computed from the RMS amplitude at each aerostat position relative to the YIF4 ground station and then plotted at the appropriate azimuth (clockwise from north) and takeoff angle (from edge to center). Blue arrow is the wind vector.

sparse. Hence, the observed radiation anomaly is featured in both discrete impulsive events and extended low-level (tremor like) eruption activity.

We next confirm that the amplitude ratios (Figure 3) are also represented in individual example waveforms. We observe a range of eruption types expressed in the acoustic data (Figure 4) including short impulsive events (Figures 4a and 4b), tremor bursts (Figures 4c and 4d), and larger impulses both with (Figures 4e, 4g, and 4h) and without (Figure 4f) high-frequency codas. Short impulses, tremor bursts, and high-frequency impulses are observed at both craters, but the low-frequency impulse (Figure 4f) seems to be unique to the S Crater over the short aerostat deployment period. Video footage for events shown in Figures 4d–4f show that the tremor bursts reflect low-level eruptive activity which may last for several tens of seconds. Short impulses (Figures 4a and 4b) may represent pulsatory activity that is sometimes audible at similar time scales to the acoustic record. The two example waveforms for Figures 4e and 4f are shown as still images in Figures 2a and 2b, as well as in the supporting information Movies S3 and S4. For these cases, the video records show quite similar impulsive eruptions while the resulting waveforms differ. This distinction implies that in some cases, very different waveform characteristics may be expressed visually with similar eruption features, highlighting the importance of careful characterization as outlined in Spina et al. (2016) and Meier et al. (2016). Indeed, the S vent eruption (Figure 2b and supporting information Movie S4) occurs during a period when the vent is badly obscured by prior ash eruptions and the vent conditions cannot be readily observed. Similar event types have been distinguished in the prior acoustic studies at Yasur (Meier et al., 2016; Spina et al., 2016) with small and large eruption events (Figure 4) being represented in the earlier work.

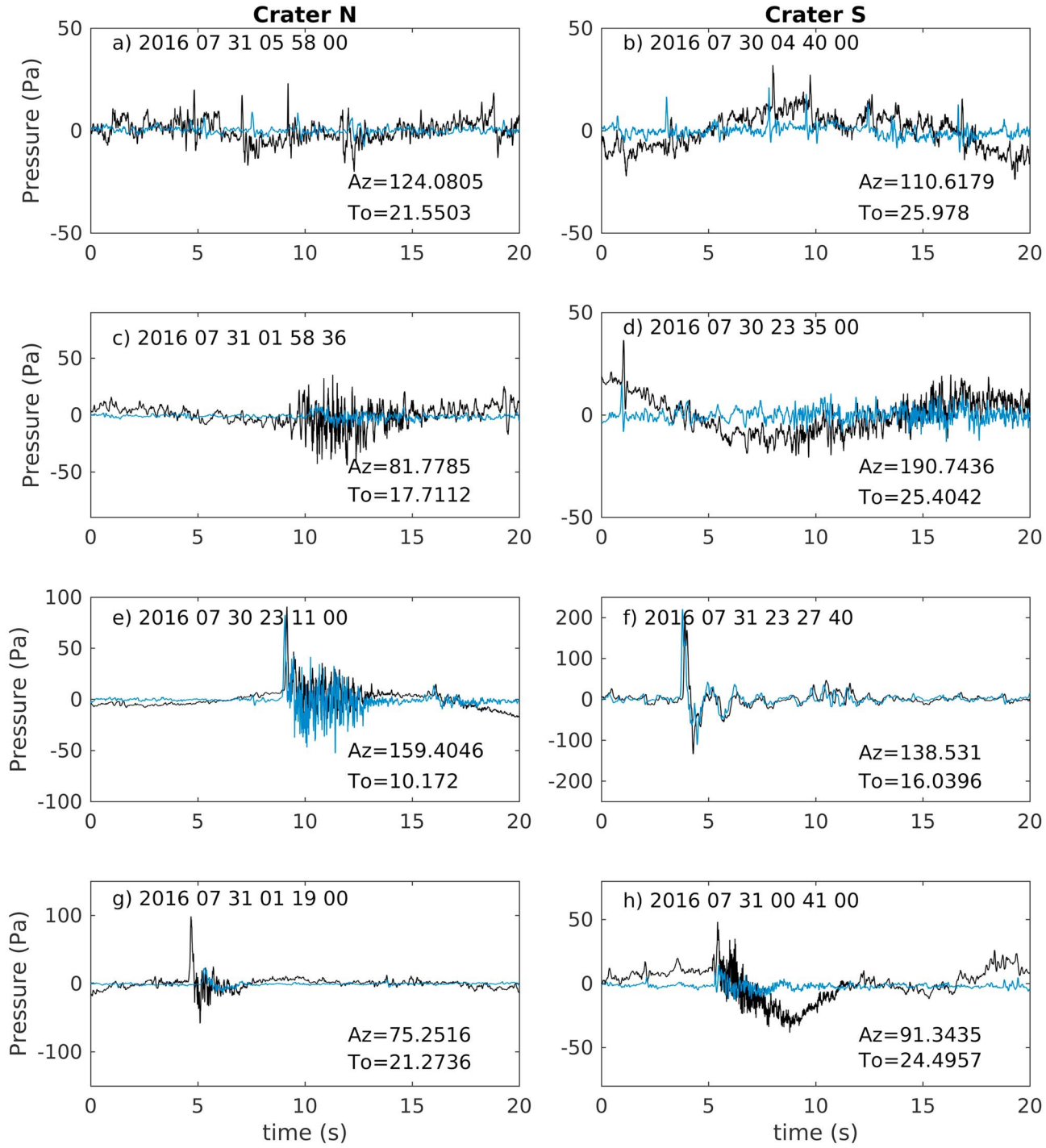

Figure 4. Waveforms for aerostat sensor (AC7-2, black) and ground sensor (YIF4, blue) showing commonly observed acoustic event types including (a, b) small impulses, (c, d) bursts, and (e, h) large impulses. Example events showing (e and f) low-amplitude ratios compared to (c, g, and h) high-amplitude ratios. The waveforms are unfiltered and have not been time migrated. Note the labeled azimuth (Az) and takeoff angle (To) for the two event types. The images in Figures 2a and 2b correspond to waveforms shown in Figures 4e and 4f and are drawn from supporting information Movie S3 (N Crater) and supporting information Movie S4 (S Crater).

The variable radiation patterns seen in Figure 3 and confirmed in the example waveforms shown in Figure 4, with strong amplitude differences for waveforms shown in Figures 4c, 4g, and 4h compared to those shown in the other figures (compare YIF4 (blue waveforms) to AC7 aerostat data (black waveforms)).

5. Discussion and Conclusions

We observe systematic variations in the acoustic radiation pattern at Yasur volcano over a 4 day study period (Figure 2). Before assessing the range of processes that might produce the observed patterns, we first examine the errors and uncertainties in the data. We note that the results appear to be persistent regardless of the size threshold used or when substituting triggered for continuous data. In addition, the aerostat sensor location and vent position may introduce uncertainties in the azimuth and takeoff angle computed in Figure 3. For example, uncertainties in the vent position depth, as determined from laser ranging of the vent described in section 2, are probably of the order of 15 m and hence are similar to the uncertainties outlined for the aerostat sensor altitude. These uncertainties are expressed as systematic shifts in the takeoff angle of ~5°. Errors for aerostats lateral position are of a similar scale (section 3) which suggests lateral azimuthal uncertainties that are ~3°. The anomalous eastward directed radiation pattern (Figures 3c and 3d), which spans an azimuth and incidence range of 50° to 100°, is much more extensive than the aspect (azimuth and takeoff angle) uncertainties and therefore, would not result from a systematic location artifact.

Site effects may have considerable impact on the observed eruption radiation pattern. High noise levels from airborne sensors were particularly notable (Figure 4). We regard these noise characteristics as a direct result of wind shear on the sensor-aerostat-tether platform. At higher frequencies, we noted audible flutter of the aerostat and vibrations in the tether line. We also noted a periodic long-period oscillation that is observed on the lowest sensor on the array string (Figures 4b and 4d) which were probably due to pendulum oscillation of the sensor string. These effects were minimized by band-pass filtering prior to calculation of the amplitude ratios in Figure 3d.

Topographic barriers (e.g., Lacanna et al., 2014), which are capable of reflecting and diffracting acoustic impulses, are important contributors to the distortion and amplification of the acoustic wavefield. In our case, the western crater wall (Figure 1a) is 40–50 m higher than in other azimuthal directions which may focus the eruption energy onto the eastern side of the volcano. We do note, however, that the primary first impulses shown in Figure 4 have the same AC7/YIF4 amplitude ratios as for their lower amplitude codas. We surmise that the first impulse would be less influenced by scattering (e.g., Woulff & McGetchin, 1976) and possibly included stronger influence from source directivity features.

In addition to topographic effects, the atmospheric state influences infrasound propagation. At the source-receiver distances considered here, infrasound propagation near volcanoes is primarily influenced by vertical gradients in temperature and horizontal winds in the boundary layer, including their microscale interactions with volcanic topography (e.g., Fee & Garces, 2007; Johnson et al., 2012; Lacanna et al., 2014; Marcillo & Johnson, 2010; Matoza et al., 2009). In our case, the persistent wind from the east-southeast (Figure 2g) implies downwind focusing and higher downwind amplitudes (e.g., Lacanna et al., 2014), opposite from the pattern observed (Figures 3c and 3d).

Finally, the observed radiation anomaly may be plausibly related to source directivity features from an eastward angled dipole source. The observed directivity pattern for larger ballistic eruptions (Figure 1e) are generally consistent with this observation but future work incorporating numerical wave propagation modeling and high-speed visual and infrared imaging is required to shed more light on source directivity at Yasur. Future improvements to the present experiment may focus on simultaneous collection of data from multiple aerostats, and the collection of data over longer time periods. The latter may emphasize data capture over a wider range of wind speeds and directions which in turn would allow denser sampling of the acoustic wavefield. These efforts may be able to distinguish the radiation patterns of specific and commonly occurring waveform features.

Acknowledgments
This work was funded by GNS Strategic Development Fund to A. J. and R. J. and New Zealand Strategic Science Investment Funding (SSIF) to A. J., B. K., R. F., and R.J. The National Science Foundation funded D. F. (EAR 1331084) and R. M. (EAR-1620576). B. K. and R. F. acknowledge New Zealand Earthquake Commission EQC Biennial grant (16/727). Janvion Cevuard, Athanase Worwor, Julius Mala, Bruce Christenson, Di Christenson, Geoff Kilgour, Nick Key, Adrien Tessier, Esline Garaebiti, and Sandrine Cevuard supported the field-work. Tony Hurst and John Ristau reviewed the early manuscript and Mie Ichihara, and an anonymous reviewer provided valued journal reviews. Limited data derived from this experiment are available in supporting information S5.

References

Battaglia, J., Metaxian, J., & Garaebiti, E. (2016). Families of similar events and modes of oscillation of the conduit at Yasur volcano (Vanuatu). *Journal of Volcanology and Geothermal Research*, *322*, 196–211. https://doi.org/10.1016/j.jvolgeores.2015.11.003

Banister, J. R., & Hereford, W. V. (1991). Observed High-Altitude Pressure Waves From an Underground and a Surface Explosion. *Journal of Geophysical Research*, *96*(D3), 5185–5193.

Bowman, D. C., Taddeucci, J., Kim, K., Anderson, J. F., Lees, J. M., Graettinger, A. H., Sonder, I., & Valentine, G. A. (2014). The acoustic signatures of ground acceleration,gas expansion and spall fallback in experimental volcanic explosions. *Geophysical Research Letters*, *41*, 1916–1922. https://doi.org/10.1002/2014GL059324

Fee, D., & Garcés, M. (2007). Infrasonic tremor in the diffraction zone. *Geophysical Research Letters*, *34*, L16826. https://doi.org/10.1029/2007GL030616

Fitzgerald, R. H., Tsunematsu, K., Kennedy, B. M., Breard, E. C. P., Lube, G., Wilson, T. M., … Cronin, S. J. (2014). The application of a calibrated 3D ballistic trajectory model to ballistic hazard assessments at Upper Te Maari, Tongariro. *Journal of Volcanology and Geothermal Research*, *286*, 248–262. https://doi.org/10.1016/j.jvolgeores.2014.04.006

Fournier, N., & Jolly, A. D. (2014). Detecting complex eruption sequence and directionality from high-rate geodetic observations: The August 6, 2012 Te Maari eruption, Tongariro, New Zealand. *Journal of Volcanology and Geothermal Research*, *286*, 387–396. https://doi.org/10.1016/j.jvolgeores.2014.05.021

Ichihara, M., Takeo, M., Yokoo, A., Oikawa, J., & Ohminato, T. (2012). Monitoring volcanic activity using correlation patterns between infrasound and ground motion. *Geophysical Research Letters*, *39*, L04304. https://doi.org/10.1029/2011GL050542

Johnson, J. B., Aster, R. C., Ruiz, M. C., Malone, S. D., McChesney, P. J., Lees, J. M., & Kyle, P. R. (2003). Interpretation and utility of infrasonic records from erupting volcanoes. *Journal of Volcanology and Geothermal Research*, *121*(1–2), 15–63.

Johnson, J. B., Anderson, J., Marcillo, O., & Arrowsmith, S. (2012). Probing local wind and temperature structure using infrasound from Volcan Villarrica (Chile). *Journal of Geophysical Research-Atmospheres*, *117*, D17107. https://doi.org/10.1029/2012JD017694

Johnson, J. J., & Aster, R. C. (2005). Relative partitioning of acoustic and seismic energy during Strombolian eruptions. *Journal of Volcanology and Geothermal Research*, *148*, 334–354.

Jolly, A., Jousset, P., Lyons, J., Carniel, R., Fournier, N., Fry, B., & Miller, C. (2014). Seismo-acoustic evidence for an avalanche driven phreatic eruption through a beheaded hydrothermal system: An example from the 2012 Tongariro eruption. *Journal of Volcanology and Geothermal Research*, *286*, 331–347. https://doi.org/10.1016/j.jvolgeores.2014.04.007

Jolly, A. D., Kennedy, B., Edwards, M., Jousset, P., & Scheu, B. (2016). Infrasound tremor from bubble burst eruptions in the viscous shallow crater lake of White Island, New Zealand, and its implications for interpreting volcanic source processes. *Journal of Volcanology and Geothermal Research*, *327*, 585–603. https://doi.org/10.1016/j.jvolgeores.2016.08.010

Kanamori, H., & Given, J. W. (1982). Analysis of long-period seismic waves excited by the May 18, 1980, eruption of Mount St. Helens—A terrestrial monopole? *Journal of Geophysical Research*, *82*(B7), 5422–5432. https://doi.org/10.1029/JB087iB07p05422

Kieffer, S. W. (1981). Blast dynamics at Mount St. Helens on 18 May 1980. *Nature*, *291*, 568–570.

Kim, K., Fee, D., Yokoo, A., & Lees, J. M. (2015). Acoustic source inversion to estimate volume flux from volcanic explosions. *Geophysical Research Letters*, *42*, 5243–5249. https://doi.org/10.1002/2015GL064466

Kremers, S., Wassermann, J., Meier, K., Pelties, C., van Driel, M., Vasseur, J., & Hort, M. (2013). Inverting the source mechanism of Strombolian Explosions at Mt. Yasur, Vanuatu, using a multi-parameter dataset. *Journal of Volcanology and Geothermal Research*, *262*, 104–122.

Lacanna, G., & Ripepe, M. (2013). Influence of near-source volcano topography on the acoustic wavefield and implication for source modelling. *Journal of Volcanology and Geothermal Research*, *250*, 9–18. https://doi.org/10.1016/j.jvol-geores.2012.10.005

Lacanna, G., Ichihara, M., Iwakuni, M., Takeo, M., Iguchi, M., & Ripepe, M. (2014). Influence of atmospheric structure and topography on infrasonic wave propagation. *Journal of Geophysical Research: Solid Earth*, *119*, 2988–3005. https://doi.org/10.1002/2013JB010827

Lighthill, J. (1978). *Waves in fluids* (2nd ed.). Press, Cambridge, U. K.: Cambridge University.

Lighthill, M. J. (1952). On sound generated aerodynamically: I. General theory. *Proceedings of the Royal Society of London, Series A*, *211*, 564–581.

Lighthill, M. J. (1954). On sound generated aerodynamically: II. Turbulence as a source of sound. *Proceedings of the Royal Society of London, Series A*, *222*, 1–32.

Lighthill, M. J. (1962). The Bakerian Lecture, 1961: Sound generated aerodynamically. *Proceedings of the Royal Society of London, Series A*, *267*(1329), 147–182.

Lube, G., Breard, E. C. P., Cronin, S. J., Proctor, J. N., Brenna, M., Moebis, A., … Fournier, N. (2014). Dynamics of surges generated by hydrothermal blasts during the 6 August 2012 Te Maari eruption, Mt. Tongariro, New Zealand. *Journal of Volcanology and Geothermal Research*, *286*, 348–366. https://doi.org/10.1016/j.jvolgeores.2014.05.010

Marcillo, O., & Johnson, J. B. (2010). Tracking near-surface atmospheric conditions using an infrasound network. *The Journal of the Acoustical Society of America*, *128*(1), EL14–EL19. https://doi.org/10.1121/1.3442725

Marcillo, O., Johnson, J. B., & Hart, D. (2012). Implementation, characterization, and evaluation of an inexpensive low-power low-noise infrasound sensor based on a micromachined differential pressure transducer and a mechanical filter. *Journal of Atmospheric and Oceanic Technology*, 29.

Matoza, R. S., Fee, D., Neilsen, T. B., Gee, K. L., & Ogden, D. E. (2013). Aeroacoustics of volcanic jets: Acoustic power estimation and jet velocity dependence. *Journal of Geophysical Research: Solid Earth*, *118*, 6269–6284. https://doi.org/10.1002/2013JB010303

Matoza, R. S., Garces, M. A., Chouet, B. A., D'Auria, L., Hedlin, M. A. H., De Groot-Hedlin, C., & Waite, G. P. (2009). The source of infrasound associated with long-period events at Mount St. Helens. *Journal of Geophysical Research: Solid Earth*, *114*, B04305. https://doi.org/10.1029/2008JB006128

McKee, K., Fee, D., Yokoo, A., Matoza, R. S., & Kim, K. (2017). Analysis of gas jetting and fumarole acoustics at Aso Volcano, Japan. *Journal of Volcanology and Geothermal Research*, *340*, 16–29. https://doi.org/10.1016/j.jvolgeores.2017.03.029

Meier, K., Hort, M., Wassermann, J., & Garaebiti, E. (2016). Strombolian surface activity regimes at Yasur volcano, Vanuatu, as observed by Doppler radar, infrared camera and infrasound. *Journal of Volcanology and Geothermal Research*, *322*, 184–195. https://doi.org/10.1016/j.jvolgeores.2015.07.038

Métrich, N., Allard, P., Aiuppa, A., Bani, P., Bertagnini, A., Shinohara, H., … Massare, D. (2011). Magma and volatile supply to postcollapse volcanism and block resurgence in Siwi caldera (Tanna Island, Vanuatu arc). *Journal of Petrology*, *52*, 1077–1105.

Nairn, I. A., Scott, B. J., & Giggenbach, W. F. (1988). Yasur volcano investigations, Vanuatu, Sept 1988. *New Zealand Geological Survey Report G*, *136*, 1–74.

Oppenheimer, C., Bani, P., Calkins, J. A., Burton, M. R., & Sawyer, G. M. (2006). Rapid FTIR sensing of volcanic gases released by Strombolian explosions at Yasur volcano, Vanuatu. *Applied Physics B: Lasers and Optics*, *85*, 453–460.

Pierce, A. D. (1989). *Acoustics: An introduction to its physical principals and applications*. Melville, N. Y: Acoustical Society of America.

Rowell, C. R., Fee, D., Szuberla, C. A. L., Arnoult, K., Matoza, R. S., Firstov, P. P., … Makhmudov, E. (2014). Three-dimensional volcano-acoustic source localization at Karymsky Volcano, Kamchatka, Russia. *Journal of Volcanology and Geothermal Research*, *283*, 101–115. https://doi.org/10.1016/j.jvolgeores.2014.06.015

Spina, L., Taddeucci, J., Cannata, A., Gresta, S., Lodato, L., Privitera, E., … Palladino, D. M. (2016). Explosive volcanic activity at Mt. Yasur: A characterization of the acoustic events (9–12th July 2011). *Journal of Volcanology and Geothermal Research*, *322*, 175–183. https://doi.org/10.1016/j.jvolgeores.2015.07.027

Tsunematsu, K., Ishimine, Y., Kaneko, T., Yoshimoto, M., Fujii, T., & Yamaoka, K. (2016). Estimation of ballistic block landing energy during 2014 Mount Ontake eruption. *Earth, Planets and Space*, *68*, 88.

Woulff, G., & McGetchin, T. (1976). Acoustic noise from volcanoes: Theory and experiment. *Geophysical Journal of the Royal Astronomical Society*, *45*, 601–616.